# In Vivo flow and wall shear stress assessment in the carotid artery with MRI

Box, F.M.A.

# Chapter 6

---

# Patient Specific Imaging for Computational Fluid Dynamical Calculations with MRI

Frieke MA Box, Patrick JH de Koning, Rob J van der Geest, Joost Doornbos, Marcel CM Rutten, Rogier M Bertina, Mark A van Buchem, Johan HC Reiber

From the Division of Image Processing (F.M.A.B., P.J.H.K., R.J.vd G., J.H.C.R.) of the Department of Radiology (J.D., M.A.v B.), of the Department of Hematology, Ctr Hemostasis & Thrombosis Res (R.M.B.), Leiden University Medical Center, Leiden, and from the Department of Biomedical Engineering, Eindhoven University of Technology, Eindhoven (M.C.M.R.), The Netherlands

Submitted

**Abstract**

In regions where the mechanical drag force per unit area of the flowing blood on the endothelial wall, the so-called Wall Shear Stress (WSS), is low or oscillating, plaque development occurs. Modern non-invasive MRI techniques combined with fluid dynamic assessments provide objective information about the presence, extent and severity of WSS distortions in a 3D-visualization of major vessels. In this article an overview is given of our research in patient specific imaging with MRI in combination with Computational Fluid Dynamics (CFD) directed at the assessment of the local WSS.

## 6.1 Introduction

The 3D geometry of vessels, such as the carotid arteries, and the 3D velocity profiles therein can be assessed nowadays in a non-invasive manner using Magnetic Resonance Imaging (MRI) techniques. Applying finite element computations from the fluid dynamics field to such geometries allows the assessment of the presence, extent and severity of wall shear stress (WSS) distortions. The WSS is the mechanical force per unit area exerted by the flowing blood on the vessel wall. Disturbance of the WSS and the Wall Shear Rate (WSR) distribution within a vessel is believed to be one of the key factors in the development of atherosclerosis [1]. The WSS (Pa) is defined by the WSR ($s^{-1}$) multiplied by the dynamic blood viscosity $\eta$ (Pa.s): Near the vessel wall, the WSR can be expressed as the fluid velocity gradient with respect to the outward normal n of the wall, or in other words

$$WSS = \eta WSR = \eta \partial v/\partial n, \qquad (1)$$

with v being the fluid velocity [m/s].
Worldwide there is a lot of interest in studying the possible relations between WSS abnormalities and the atherosclerotic process. Non-invasive detection of WSS distortions may be clinically of great interest to be able to initiate preventive therapy in selective patient populations with high-risk profiles. So far most of these studies have been carried out using echo-Doppler [2, 3, 4]. However, normally echo-Doppler is a 2D-technique with a limited scan window and therefore only applicable to certain vessels located at the surface of the body, and the technique is highly observer-dependent. In addition, it only allows the assessment of the highest velocity values in a vessel and not the full velocity profile. Finally, WSS values can be derived in regions with forward flow, not at the local level where plaque development occurs, making it a lot less of interest.
Since a number of years, Magnetic Resonance Imaging (MRI) has been developed as a novel and widely applicable three-dimensional imaging modality, allowing a non-invasive and accurate assessment of vessel morphology and blood flow velocity in all vessels, also those located deeper inside the body. Another advantage: it is not harmful to the patient so that acquisition procedures can be repeated without any problem and with good geometric reproducibility. Combined with accepted methods from fluid dynamics theory and Finite Element Methods (FEM), MRI allows the accurate in-vivo quantification of the *local* WSS [5, 6].

For the assessment of the local WSS, the FEM method demands boundary conditions. The boundary conditions are formed by the 3D geometry of the vessel wall and the blood flow at the in- and outflow locations of the simulated vessel part. The geometry of the vessels, the blood flow and the blood viscosity differ widely between individuals. Therefore, a method to achieve reliable patient specific data is necessary. In our division, a software package (MRA-CMS) has been developed for the automated segmentation and visualization of arteries from 3D MR angiographic data [7]. These 3D data sets, representing the surface of the vessel wall can be used to form the vessel wall boundary condition in the finite element method. The other necessary boundary conditions, the in- and outflow, can be assessed with velocity encoded MRI. A method was developed to assess blood flow during the various phases in the cardiac cycle. This method provides blood flow data in a precise and reproducible manner from the cross-sectional velocity profiles in the internal carotid and vertebral arteries [8].

The outline of this paper is as follows. In section 2.1 to 2.4 the used materials and methods are discussed. In particular, in section 2.1, the segmentation method of vessel geometries assessed with Magnetic Resonance Angiography (MRA) will be discussed. The assessment of the in- and outflow conditions with velocity encoded MRI is presented in section 2.2. Next, the simulation by FEM is described in section 2.3. A validation method, which compares the measured and calculated flow and velocity profiles, is presented in section 2.4. The results of the validation studies of the various sections are subsequently presented in section 3. Finally, in the discussion (section 4) a bird's eye overview of the current technology is given and expectations for the future are described. In conclusion, this simulation pipeline opens up new possibilities for CFD applications like the assessment of patient specific WSS distributions in vessels anywhere in the body (figure 1).

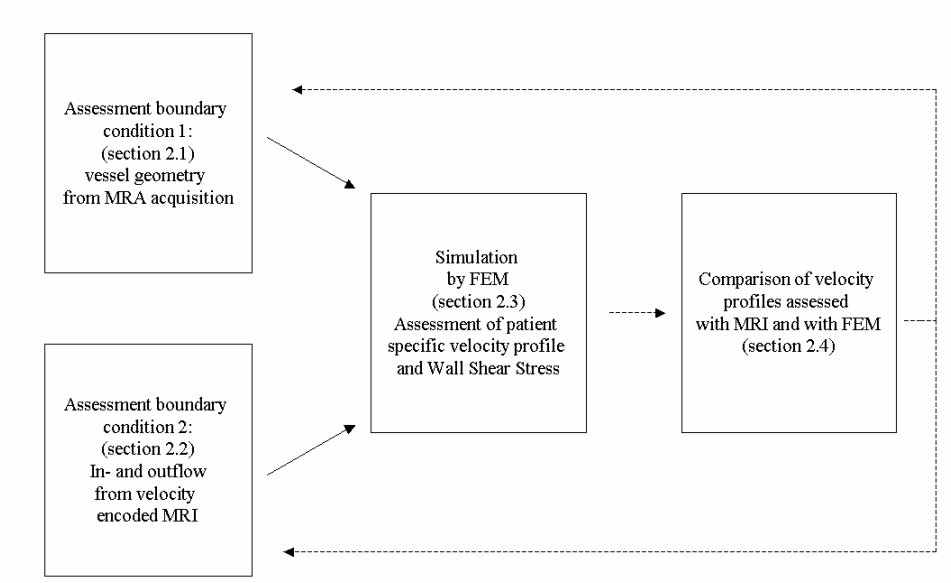


**Figure 1.** Schematic overview of the pipeline to assess WSS data based on patient specific imaging. The dashed lines are not discussed in this article.

## 6.2 Materials and Methods

### 6.2.1 Vessel geometry segmentation and imaging with MRI

Contrast enhanced (CE) Magnetic Resonance Angiography (MRA) provides 3D images of the morphology of the blood vessels in the body. Visual interpretation of these 3D images is usually carried out using 2D projection images called Maximum Intensity Projections (MIP). However, these MIPs contain less information, because all information in the 3D space is compressed into a 2D image. This results also in over-projection of vessels, requiring again visualization and therefore recalculations of MIPs from multiple views. Without advanced analytical software, the value of MRA is limited and this advanced technology cannot be used to its full potential. In our division we have developed

analytical software for the quantitative analysis of MRA data sets. Technical details of the software structure and the segmentation algorithms were described by de Koning et al. [7]. In brief, the user defines a start and end point on the vessel to be analyzed in the 3D data space. A 3D pathline is then automatically detected through the vessel segment connecting these points. The 3D pathline detector is based on the fast marching level set method (FMLSM), as described previously [9]. The FMLSM numerically approximates the propagation of a wavefront through a medium and computes the arrival time of the wavefront at each image element. In order to minimize inter- and intra-user variability, an automated method is used to determine all of the settings of the FMLSM. After calculation of the centerline in 3D, the vessel lumen must be detected. This is achieved by applying the 3D extension of the full width at 30% maximum (FW30%M) criterion [10]. This method thresholds the image at 30% of the intensity of the center lumen line. After these segmentation processes and 3D reconstruction of the vessel, the cross-sections (in $mm^2$) along the vessel pathway are calculated and the percent area-stenosis of a particular narrowing can be deduced; if necessary percent diameter-stenosis can also be derived assuming a circular cross section.
This method was applied on *in vitro* data, which consisted of CE-MRA studies of five flexible polyolefin heat shrink tube phantoms, which were placed in a stationary flow circuit [10]. These five phantoms all had identical reference diameters (6.80 mm) and different obstruction diameters (1.97, 2.92, 3.47, 4.69 and 5.58 mm).
De Vries et al [11] have shown that the semi-automated evaluation of aorto-iliac 3D CE-MRA has the same high accuracy for significant stenosis detection and quantification as conventional readings of CE-MRA.

### 6.2.2 The assessment of in- and outflow with MRI

Once the geometry of the vessel is known, the in- and outflow distributions are required for the subsequent assessment of the velocity profiles and the derived WSS distributions along that vessel segment. To achieve the correct in-and outflow data, a description of the cross-sectional velocity profiles at these places is necessary. To that end, we developed and validated a fast, semi-automatic and user-independent automatic fitting approach, which is relatively simple to implement on each MR-machine and flow-protocol. It is based on a standard MR blood flow acquisition protocol, yielding accurate and reproducible flow data [12]. It was assumed that a parabolic flow velocity profile is a valid model for the blood flow in vessels with a small diameter and a relatively constant flow rate over the cardiac cycle. The proposed automatic approach, therefore, is based on the fitting of a three-dimensional parabolic velocity profile to the actual velocity data, thus providing boundary conditions of the vessel of interest. The accuracy and reproducibility of this new automatic flow assessment approach was evaluated and compared to the conventional manual analyses using phantom and in-vivo studies [8].

### 6.2.3 Flow acquisition with MRI

The MR examinations were performed on a 1.5 T scanner (Gyroscan NT; Philips Medical Systems, Best, the Netherlands) using a standard head coil. A gradient echo phase contrast imaging sequence was applied using retrospective cardiac gating by means of a peripheral pulse unit, resulting in 16 phases over the cardiac cycle. The imaging parameters were: TE 9 ms, TR 16 ms, 7.5° flip angle, 5 mm slice thickness, 250 × 180 mm field of view (FOV), scan matrix 256 × 154 pixels and a velocity sensitivity of 100 cm/s. The scan time was dependent on the heart rate, being 3 minutes at 60 beats/min. Scans were acquired perpendicular to the major flow direction of the vessels and tubes.

### 6.2.4 Fitting the flow profile

The cross section of the vessel was assumed to be circular and the velocity profile to be parabolic. A paraboloid (eq 2) was fitted to the measured velocity profiles using the following formula

$$u(x,y) = A*(x^2 + y^2) + Bx + Cy + D, \qquad (2)$$

where u(x,y) is the velocity value at position (x,y) and A,B,C and D are fitting parameters. The velocity profile was averaged over the cardiac cycle and was fitted to the paraboloid. The pixels for which the fitted parabolic velocity profile had positive values, were included in the region-of-interest (ROI). The individual flow values per phase of the cardiac cycle were obtained by the multiplication of the average velocity of the pixels within the ROI at that phase in the cardiac cycle, multiplied by the area of the ROI [8].

### 6.2.5 Manual contour definition procedure

For validation purposes, the data was also compared with manually segmented vessels, being referred to as the conventional method or gold standard. Each acquisition run was analyzed manually in an independent manner by 7 experienced observers. The group of observers consisted of one radiologist and six image processing scientists with experience in MRI. They were instructed to segment the image in the following manner: the delineation of the vessel contour was carried out on an enlarged image of one time bin (one phase in the cardiac cycle). First, the observer selected the phase within the cardiac cycle characterized visually by the highest contrast in the image. The observers were advised to use images obtained during systole. Next, the observer drew manually a region of interest (ROI) in the vessel. Finally, this ROI was copied to the 15 remaining phases within the cardiac cycle. The instantaneous flow values were calculated by multiplication of the measured velocities inside the ROI times the area of the ROI.

### 6.2.6 Phantom study

To determine the accuracy and reproducibility of the flow measurements, a small phantom study was carried out. The phantom consisted of three straight glass tubes with inner diameters of 5, 8 and 9 mm, respectively and a length of 20 cm connected to a programmable pulsatile pump which delivered a physiological waveform (Shelley Medical Imaging Technologies, London, Ontario, Canada). The flow volume delivered by the pump was set at 551.76 ml/min (9.196 ml/s). The flow curve as a function of time was typical for a carotid artery and had an amplitude of 30 ml/s. The liquid was a mixture of water (60%) and glycerol (40%), so that the viscosity was comparable to that of blood (4.3 mPas). The systematic errors were defined by: measured - true flow rate.

### 6.2.7 *In vivo* study

In addition, an in vivo study was carried out. The study population consisted of 8 healthy volunteers (aged 20-30 years, 3 women and 5 men). Flow velocities in the vertebral and internal carotid arteries were assessed in a plane perpendicular to these arteries at different positions in the neck. For the internal carotid artery a slice location 4 cm distal of the bifurcation was selected, and for the vertebral artery 2 cm proximal to the pars atlantica. For each vessel the acquisition procedure was repeated three times. To assess the stability of flow measurements (re-examination) on a given MR system, a second scan was performed directly after the first one, while the volunteer stayed inside the MR scanner. To

assess the influence of repositioning a patient in the MR system, which may give rise to variation in location and angle of the flow measurement, a third acquisition procedure was performed after the volunteer came out of the machine and was repositioned inside the scanner. For the third scan, new plan scans were set and the flow measurement was based on these new plan scans. The total cerebral blood flow (TCBF) was calculated by adding the flow through the two ICA's and the two vertebral arteries.

### 6.2.8 Statistical analyses

The Intra Class Correlation (ICC) analysis was used to describe the degree of reproducibility [13]. Also the 95% reliability interval of the ICC was determined. Note that the automatic method has no inter- or intra- observer variability associated with it. The only user-interaction is that the user has to indicate the correct vessel by a click of the mouse.

### 6.2.9 Simulation by the FEM method based on MR measurements

Local WSS can be calculated by using a Finite Element Method (FEM). We used a well-tested model, the Carreau-Yasuda model for non-Newtonian viscosity. We investigated the influence of hematocrit (Hct), plasma viscosity and the flow rate on the WSS. The hematocrit levels (Hct) were varied within ranges, which were obtained from a group of 20 healthy volunteers (Hct range: 0.346-0.506). This study was based on *in vitro* measurements using a carotid artery bifurcation model, and on *in vivo* measurements in a group of 20 healthy young volunteers, 10 men and 10 women. Measurements of the three volunteers with the lowest Hct, the average and with the highest Hct, respectively were selected for further analysis.

### 6.2.10 Phantom model and MRI acquisitions

A phantom model of the carotid bifurcation was constructed of polymethyl methacrylate and had an inflow diameter of 8 mm. The outflow diameters were 5.6 and 4.6 mm, for the internal carotid and external carotid arteries, respectively. The model was connected to a straight tube and a MRI compatible pump (Shelley Medical Imaging Technologies), which can deliver an adjustable (pulsatile) flow profile flow(t). The geometry was obtained by means of a MR angiographic acquisition protocol. The acquired phantom data was divided into 100 slices with a slice thickness of 1 mm, a TE/TR 6.8/21 ms, a field-of-view (FOV) of 256 mm, and a scan matrix of 512x512 pixels. The blood flow in the young volunteers was assessed as was described in section 2.2.

### 6.2.11 Mesh generation based on a segmented vessel

In section 2.1 the segmentation of the 3D MRA data set was described and in section 2.2 the assessment of the flow boundary conditions. In this section the current approach for the mesh generation of a 3D MRA data set will be described, in particular for a carotid bifurcation (Fig. 2a).
Each segmented vessel is expressed as a stack of cross sections, while a bifurcation is described by three vessel segments each consisting of a stack of cross sections (Fig. 2b). Figure 2c illustrates as an example the locations where the MR velocity profiles are measured. To be able to simulate the region between the measured in- and outflow cross sections, the segmented image is cut off at these positions. The cross sections of the geometry which was segmented from MRA were transformed to rectangles with the same spatial distribution as the rectangles at the surface of the mesh. Finally, the standard mesh was transformed until it matched the segmented data set (Fig. 2e) [14].

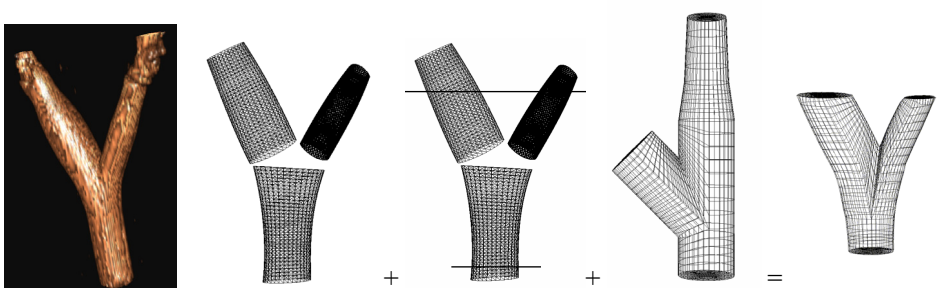

**Figure 2.**
**A,** MRA image **B,** segmented image **C,** position of velocity **D,** standard mesh **E,** matched mesh

### 6.2.12 Differential equations and method of solving

The finite element modeling approach for solving the time-dependent Navier Stokes equations and the continuity equation was used to calculate the local WSS:

$$\rho(\partial v/\partial t + ( v \bullet \nabla ) v) = -\nabla p + \nabla \bullet \eta \nabla v \qquad (3)$$
$$\nabla \bullet v = 0,$$

where v is the velocity vector, p is the pressure, ρ the blood density and η the kinematic viscosity. The elements were Crouzeix-Raviart type elements with 27 nodes, with a quadratic approximation for the three velocity components in each node. Both the pressure and the pressure gradient are defined at the centroid of each element. The package SEPRAN [15] was used to generate the mesh and to build and solve the system of equations. In this study only shear thinning properties of blood flow were taken into account; viscoelastic effects were not included. The calculations were performed on the TERAS supercomputer at SARA, Computing and Networking Services, Amsterdam, the Netherlands. TERAS is a 1024-CPU system consisting of two 512-CPU SGI Origin 3800 systems (Silicon Graphics, California).

### 6.2.13 Inflow shape adaptation

The flow through the common carotid artery of the volunteer with the lowest Hct (Flow(HctMin)), and of the volunteer with the highest Hct (Flow(HctMaxmeas)) was measured. To be able to study the effects of the flow rate on the WSR and WSS, it is important to be able to compare two flow curves with the same shape. This requires the two flow curves to be normalized in the following manner. The height of the systolic peaks is used to determine a multiplication factor for Flow(HctMin). The measured flow curve Flow(HctMaxmeas) is adapted, which gives Flow(HctMax) and is calculated as follows (see fig 3):

$$\text{Flow(HctMax)} = \{\max[\text{Flow(HctMaxmeas)}]/\max[\text{Flow(HctMin)}]\} * \text{Flow(HctMaxmeas)} \qquad (4)$$

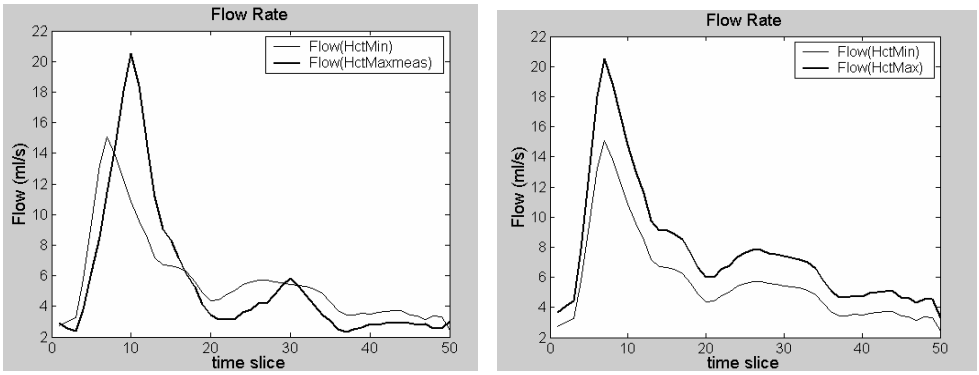


**A** **B**

**Figure 3.** **A**, The flow through the common carotid artery of the volunteer with the lowest Hct (Flow(HctMin)), and of the volunteer with the highest Hct (Flow(HctMaxmeas)). **B,** The flowcurve Flow(HctMax), where the shape of flowcurve Flow(HctMaxmeas) is adapted to flowcurve Flow(HctMin).

When the vessel geometry is available in a mesh and the flow is known, the WSS can be calculated for the different phases in the cardiac cycle (see Fig. 4).

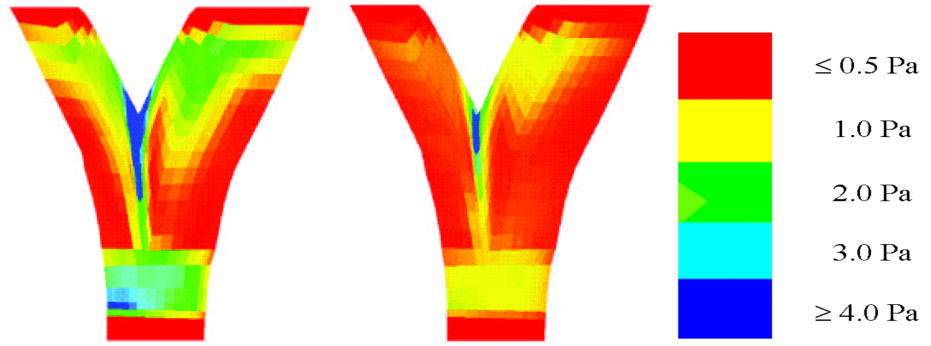


**A** **B**

**Figure 4.** WSS for peak systole (A) and mid-diastole (B). Note that the first and last elements for in- and outflow (lowest and highest positions in the figure) are colored red and are not used in the calculations of the WSS.

### 6.2.14 Blood viscosity

As discussed in the introduction, the viscosity is an important parameter for the assessment of the WSS. Blood viscosity in humans is non-Newtonian. With increasing shear rate, the viscosity decreases. These shear thinning properties can be modeled by the Carreau – Yasuda model (CY model):

$$\eta = \eta_\infty + ( \eta_0 - \eta_\infty ) [1 + \lambda_{cy}\gamma)a]^{(n-1)/a} \qquad (5)$$

where $\eta$ is the viscosity for shear rate $\gamma$, $\eta_\infty$ is the viscosity for infinite shear rate and $\eta_0$ the plasma viscosity at shear rate zero. For a well-tested blood mimicking fluid, the KSCN-X solution, $\eta_0$=22 mPa.s; $\eta_\infty$=2.2 mPa.s; a=0.644; n=0.392; $\lambda_{cy}$=0.110 s [16].

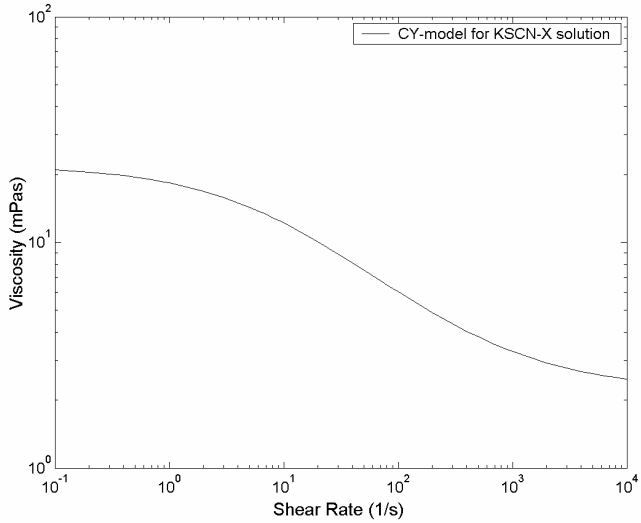


**Figure 5.** The Carreau-Yasuda model for the parameters fitted to the KSCN_X solution.

The viscosity in humans, however, can differ between individuals. Matrai has demonstrated that viscosity increases exponentially with increasing heamatocrit (Hct) [17]. Because n is placed in the exponent, we propose to replace n by Hct.
Hct and blood viscosity were measured in 20 healthy young volunteers, 10 men and 10 women. The blood viscosity was measured with a Brookfield digital viscometer (model DVII+CP). This viscometer measures blood viscosity in a reliable manner, at shear rates between 375 $s^{-1}$, and 750 $s^{-1}$. By adaptation of $\eta_\infty$, plasma viscosity can be varied. $\eta_\infty$=2.2 mPa.s was denoted high plasma viscosity and $\eta_\infty$=1.1 mPa.s low plasma viscosity. The measured viscosities in the samples with the highest, lowest and an average Hct were selected. Hct values were inserted in the CY model, and the power law index n was replaced by Hct.

### 6.2.15 Comparisons between velocity encoded MR-measurements and Finite Element Modeling in a phantom model of a curved tube

To be able to assess the local WSS distribution from MRI-images of arteries, a good approximation of the velocity profile near the vessel wall is required. One of the major drawbacks of MRI-velocity-data is the relatively low resolution and the unknown error distribution (noise). It is known that the measured flow rate can vary up to 10 % when different MR scanners are used [18]. To get around this problem, the introduced FEM calculations can be used. However, the question needs to be answered whether the calculated flow velocities along a segment of interest (tube, actual vessel, etc) agrees to a great degree with the actual acquired flow velocity values. If so MR flow velocity values can be used to optimize the boundary conditions. Also the calculation method used by FEM can be validated for *in vivo* applications. Therefore, we started with a simple curved tube model, which is a geometry that is precisely known and can be exactly modeled with FEM. Once it is demonstrated, that the measured flow and velocity profile of such an exact model are comparable to the calculations, the next step can be set towards *in vivo* validation studies. The FEM calculation for this model was previously validated by Laser Doppler Anemometry (LDA) [16]. The flow through the tube was measured by MR and

the resulting time-dependent flow-rate formed the input for the FEM calculations. The goal of this study was to determine the similarity between actually measured time-dependent flow rates (flow(t)) and velocity profiles by MRI, with the corresponding flow(t) and velocity profiles derived from FEM calculations.

## 6.3 Materials and Methods

### 6.3.1 Materials and data assessment

A PMMA (polymethyl methacrylate) phantom model of a curved tube (diameter of 8 mm) was connected to a MRI compatible pump (Shelley Medical Imaging Technologies), which can deliver an adjustable (pulsatile) flow profile flow(t). The blood emulating fluid is a Newtonian fluid with a viscosity of 2.5 mPa.s (Shelley) and MRI-compatible. The phantom was connected to a straight and fixed tube with a length of 110 cm; as a result the inflow velocity profile is known and can be described analytically (Womersley-profile) [19, 20]. The phantom was scanned with a 1.5 T MR system (Philips Medical Systems) using a standard knee-coil in two ways:

At different positions along the curved tube model, the velocity and flow values were assessed in a plane perpendicular to the major flow direction. Velocity encoded data were obtained by means of a gradient echo phase contrast imaging procedure. Triggering was applied during the acquisition and the simulated cardiac cycle was subdivided into 25 equidistant phases (time slices). The imaging parameters were: TE/TR 11.2/18.44 ms, flip angle 15 degrees, slice thickness 2 mm, FOV 150 mm, scan matrix 256x256 and velocity sensitivity 30 cm/s.

Application and validation of the SEPRAN FEM package for the analysis of cardiovascular flow has been carried out in collaboration with the Department of Biomedical Engineering at the Eindhoven University of Technology, the Netherlands [16, 21]. The mesh used for the FEM-calculations consisted of triquadratic bricks with 27 nodes [22].

The curved tube could be defined with a small extension within the mesh generator of SEPRAN.

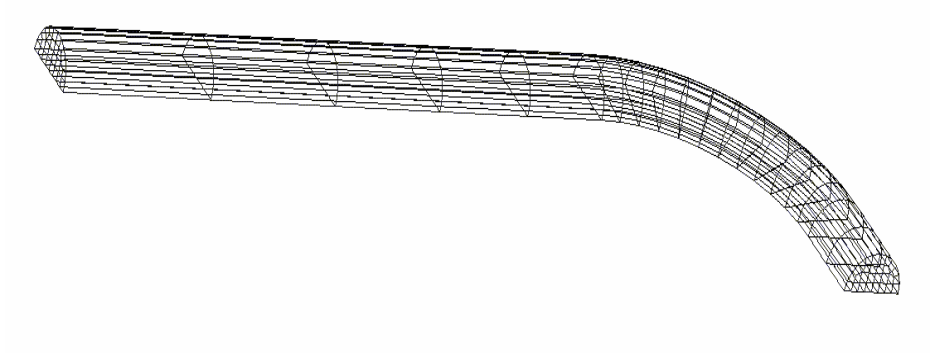

**Figure 6.** Curved tube mesh

The validation procedure consisted of a comparison between the FEM-based velocity calculations with measurements performed by Laser Doppler Anemometry (LDA).

Because of its high resolution (30 X 10 X 10 µm with 120 measurements/s ) LDA is regarded as the absolute gold standard. For comparison purposes: the MR resolution for these measurements is: 1 X 0.5 X 0.5 mm with 5 minutes scan time for 25 acquisitions.

### 6.3.2 Methods

The velocity encoded data were analyzed by means of the FLOW analytical software package [23]. FLOW allows the quantitative assessment of the velocity profiles and the subsequent calculation of the flow versus time. As described earlier, the flow was calculated by the multiplication of the average velocity in the segmented area and the surface of this area. Next, the flow in the curved tube was measured at three positions: at the entrance ($inflow_{-MR}$), in the middle ($midflow_{-MR}$) and at the exit ($outflow_{-MR}$).

The $Inflow_{-MR}$ was Fourier transformed and the first 20 Fourier coefficients were used as input in the FEM calculations. After solving the Navier-Stokes equations, the flow (in the primary flow-direction) was calculated at the position where the MR-measurement was performed ($flow_{-calc}$). For comparison purposes, $flow_{-calc}$ needs a similar grid as the MR-measurement. Therefore, a gridding and interpolation procedure was carried out on $flow_{-calc}$ which resulted in $flow_{\_image}$.
The calculated flows and velocity profiles were subsequently compared with the MR-derived flow amounts and velocity profiles. For comparison purposes between calculated and measured velocity profiles, a special option was added to the standard FLOW package. This option allows the assessment and visualization of the differences between calculated and measured velocity profiles in each phase of the cardiac cycle at each measured cross sectional position (see Fig 7).

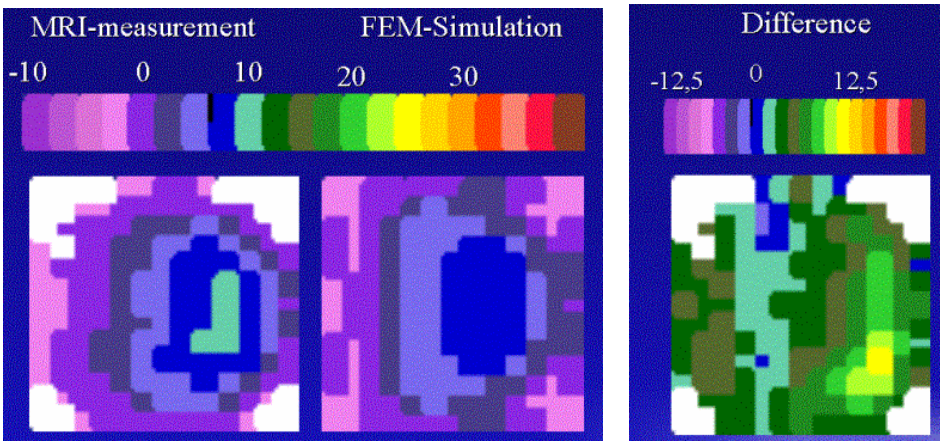


**Figure 7.** Example of a comparison between velocity profiles which was applied for all phases of the cardiac cycle based on the package FLOW. The measured or calculated 3D velocity profile is indicated by a rainbow color map, where the velocity in cm/s is indicated in the legend. The measured data (MRI-measurement) are given on the left side. The calculated velocity profile (FEM-Simulation) is given in the middle. For the differences between the two velocity profiles (Difference) another scaling is used (2*(Measurement-Simulation)). The difference is presented in the right picture.

## 6.4 Results

### 6.4.1 Validation of MRA segmentation

The correlation between the method and the true value of the phantom is excellent ($r$ = 0.995, $P$ < 0.001, $N$ = 17) (see Fig. 8). Excluding measurements smaller than 3 resolution elements improves
the correlation ($r$ = 0.999, $P$ < 0.001) In smaller vessels, such as the carotid arteries, this criterion is not always fulfilled, especially in stenotic regions. This means that the applicability of the technique will further increase with improvements in the resolution of MRA datasets.

### 6.4.2 Validation of in- and outflow assessment from velocity encoded MRI

The phantom study showed that the systematic error was -9.5 % ± 2.8 % for the manual method and -11.0 % ± 2.7 % for the automatic method [8].

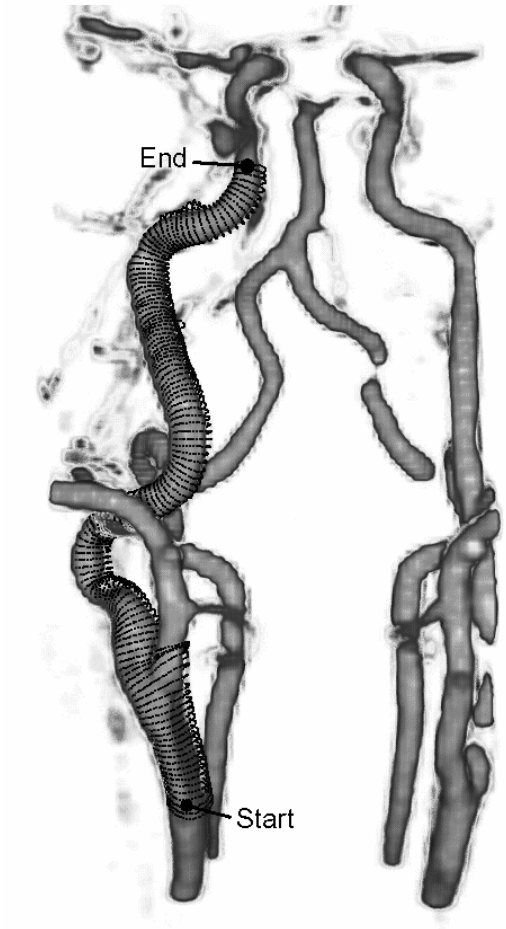


**Figure 8.** 3D reconstruction of the vessel between start and end point.

### 6.4.2.2 Re-examination and repositioning variability for TCBF

The re-examination (RE) and repositioning (RP) variability data for the internal carotid artery (ICA) and the total carotid blood flow (TCBF) are presented in Tables 1 and 2, respectively. From both tables it is evident that the automatic method performed significantly better than the manual method. The manual approach is associated with a two times higher standard deviation. However, it has to be noted that there is a significant systematic difference between the two methods of 11.0 % for the ICA. From these data it can be concluded, that flow rate can be assessed with an excellent reproducibility by MRI [8].

### 6.4.3 Results for modeling of viscosity and with the FEM method

The lowest Hct in the group of 20 volunteers was found to be 0.346, the highest was 0.506, and the average 0.432. In the shear rate range between 375 and 750 $s^{-1}$ , the Carreau-Yasuda model gives a good approximation of the viscosity for the blood of the volunteers when the power law index n is replaced by Hct (Fig 9).

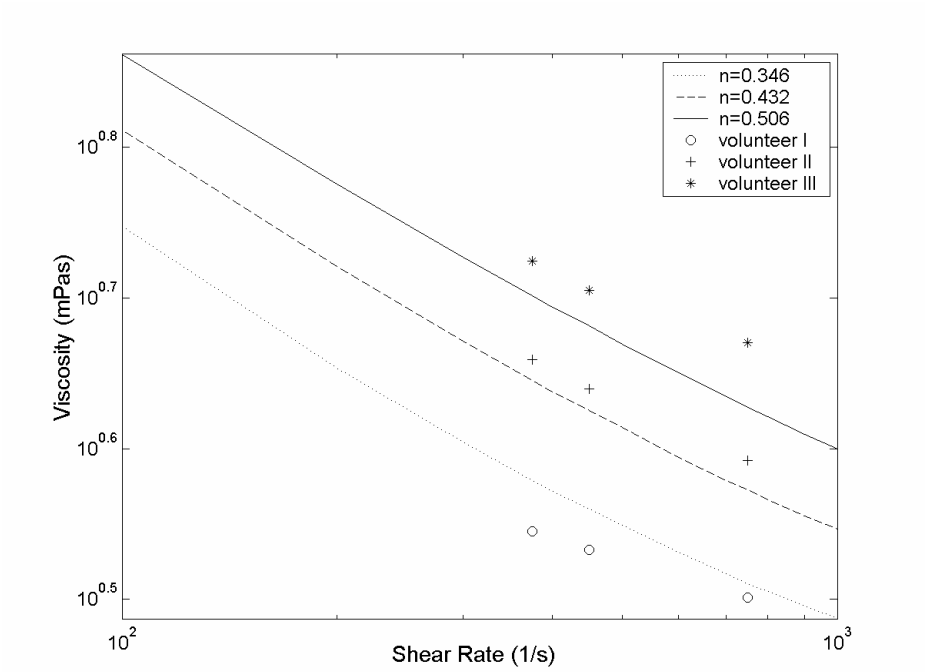


**Figure 9.** The Carreau-Yasuda model (lines) for n=Hct =0.346 (volunteer I), n=0.432 (volunteer II), n=0.506 (volunteer III) and the viscosity measurements (markers).

When all the aspects of the CFD calculation, i.e. geometry of the vessel, time-dependent blood flow and Hct are available, a patient-specific WSS calculation can be carried out. For such calculations a comparison of the WSS under different circumstances can be carried out (Fig 10). The average or mean WSS (MWSS) was calculated for two flow curves, being flow(Hctmin) and flow (HctMax) (fig 4b), and three values of Hct, being 0.346, 0.432 and 0.506.

| | Automatic Method | | | Manual Method | | | Syst diff | p-value |
|---|---|---|---|---|---|---|---|---|
| | **Mean (stdev)** | **CV (%)** | **ICC (95% rel )** | **Mean (stdev)** | **CV (%)** | **ICC (95% rel)** | | |
| **RE ICA** | 289.8 (7.5) | 2.7 | 0.97**(0.91-0.99) | 257.8 (27.2) | 11.0 | 0.90 (0.82-0.96) | 32.0 | $8.3.10^{-5}$ |
| **RP ICA** | 278.1 (12.9) | 4.3 | 0.93* (0.82-0.88) | 250.8 (27.7) | 11.1 | 0.84 (0.73-0.93) | 27.4 | $1.5.10^{-3}$ |
| **RE VA** | 109.0 (5.4) | 4.7 | 0.96* (0.87-0.99) | 101.0 (12.5) | 13.2 | 0.94 (0.89-0.98) | 8.0 | $3.5.10^{-1}$ |
| **RP VA** | 108.0 (6.6) | 5.7 | 0.95* (0.86-0.99) | 97.3 (12.4) | 14.0 | 0.94 (0.89-0.98) | 10.7 | $1.9.10^{-1}$ |

**Table 1.** The automatic method compared to the manual method for re-examination (RE) and the repositioning (RP) of individual vessels. The number of vessels was 15 for the carotids and 13 for the vertebrals. If the reproducibility was 2 stdev better it is indicated with **; if it was 1 stdev better, it is indicated with *.

| | Automatic Method | | | Manual Method | | | Syst diff | p-value |
|---|---|---|---|---|---|---|---|---|
| | **Mean (stdev)** | **CV (%)** | **ICC (95% rel )** | **Mean (stdev)** | **CV (%)** | **ICC (95% rel)** | | |
| **RE** | 720.6 (15.3) | 2.1 | 0.98**(0.95-1.0) | 646.9 (62.3) | 9.7 | 0.95 (0.89-0.99) | 73.7 | $8.5.10^{-3}$ |
| **RP** | 698.5 (27.0) | 4.2 | 0.98* (0.89-1.0) | 629.9 (63.4) | 10.2 | 0.93 (0.85-0.98) | 68.6 | $1.9.10^{-2}$ |

**Table 2.** The automatic static method for re-examination (RE) and repositioning (RP) of TCBF. The number of vessels was 15 for the carotids and 13 for the vertebrals. If the reproducibility was 2 stdev better it is indicated with **; if it was 1 stdev it is indicated with *. Abbreviations: ICA: internal carotid artery, VA: vertebral artery.

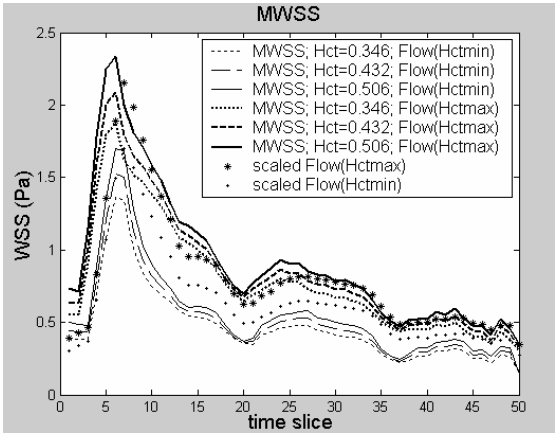


**Figure 10.** Mean-WSS during the cardiac cycle for flow curve Flow(Hctmin) and Flow(Hctmax). The flow curves are scaled at the highest WSS for the lowest flow curve Flow(HctMin) using equation 4.

From the simulations we have found that: for lower Hct, the WSR is higher. Viscosity in contrast to WSR is low for low Hct. The WSS, being the product of WSR and viscosity, decreases with decreasing Hct. It decreases also when plasma viscosity is lowered. Thus viscosity seems to be the dominant factor compared to WSR. When flow is increased, peak WSS seems to increase at a higher rate than the peak systolic flow. The mean WSS seems to increase at a lower rate than peak systolic flow. Plasma viscosity has a large influence on the WSS. When plasma viscosity is low, MWSS increases less than flow. For low plasma viscosity the WSS is more dependent on Hct. High plasma viscosity gives high PWSS [14].

### 6.4.4 Results for a comparison between a FEM simulation for a known phantom and MRI measurements

In figure 11 the flow measured by MRI is compared with $flow_{-calc}$ for the three measuring planes inflow, midflow and outflow. In figure 12 the $flow_{-image}$ is compared for different measurement planes to investigate the effects of gridding and interpolation. From Fig 11 it is evident that the outflow does not match the other measurements and calculations. Out-$FLOW_{MR}$ gives lower values in all the time slices. Other flow sites show a good agreement. A possible explanation for this discrepancy may be that the in-flow and the mid-flow were taken in the feet-head direction and the outflow in the left-right direction. Figure 12 demonstrated that gridding and interpolation do not have a significant effect on flow rate assessment.

Velocity encoded MR-measurements for the curved tube are presented together with the calculated velocity profiles at two measuring planes in figures 13 and 14. The measurements and the simulations are plotted at the plane of symmetry for the beginning, peak and end of systole, i.e. in time slice nr 20, 24 and 5, respectively (see figure 12 for the flow rate in these time slices).

The calculated velocity profiles in the curved tube show a good similarity with MR-measurements.

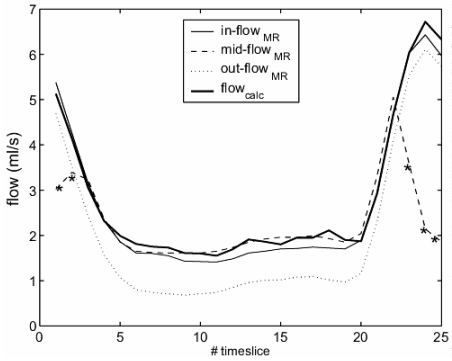


**Figure 11.** $Flow_{MR}$ and $Flow_{calc}$ for inflow, mid and outflow region of the curved tube. * Indicates a measurement error for some pixels in the measurement.

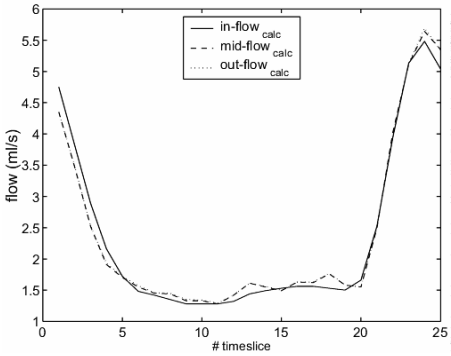


**Figure 12.** $Flow_{-image}$ for inflow, mid and outflow region of the curved tube.

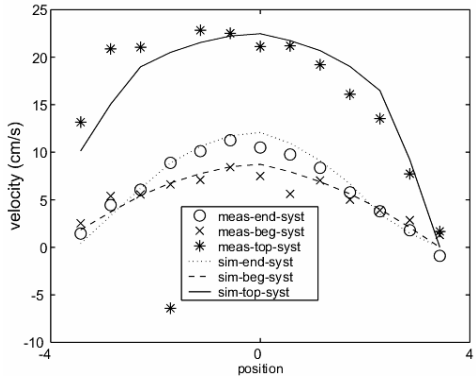


**Figure 13.** The measured and simulated velocity Velocity profiles in the direction A'-A at inflow, at the end, the beginning and at peak systole.

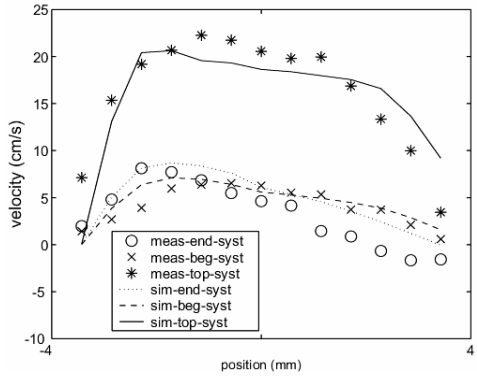


**Figure 14.** Velocity profile in the direction of A-A'at outflow, at the end, the beginning and at peak systole.

## 6.5 Discussion

Magnetic Resonance Imaging (MRI) is a three-dimensional imaging modality which allows a non-invasive and accurate assessment of vessel morphology and blood flow

velocity in all vessels, also those located deeper inside the body. Segmentation approaches for the peripheral vessels like the carotid artery were developed and applied for vessels measured with MRA (see boundary condition 1 in Fig 1) [7]. In- and outflow of a vessel segment can be assessed with velocity encoded MRI (see boundary condition 2 in Fig 1) [8]. When boundary conditions are available, blood flow can be simulated using the Finite Element method (FEM) (fig 1) [14]. The simulation pipeline can be validated by comparison of flow rate and cross sectional velocity profiles assessed by velocity encoded MRI and by FEM simulation. This approach opens possibilities for CFD applications, such as the assessment of patient-specific WSS distributions in vessels anywhere in the body. In section 3 it was shown that velocity profiles measured by velocity encoded MRI were comparable with simulated velocity profiles. This approach can be used for optimization of the boundary conditions. However, this is not discussed in this paper (see dashed line in figure 1).
We have demonstrated that the automated vessel detection in CE-MRA is able to detect the vessel lumen contour accurately, provided certain criteria regarding the acquisition are met. The required user interaction is limited to placing only a proximal and a distal point in the vessel of interest [7].

With velocity encoded MRI the flow during several phases in the cardiac cycle can be assessed with a small systematic error and an excellent reproducibility in the carotid and vertebral arteries. With this method the in- and outflow of a vessel with a diameter between approximately 2 and 6 mm outside the heart region, can be assessed in a reliable, reproducible and user independent manner [ 8, 24]. Smaller or larger vessels were not investigated in this study. Subsequently a realistic inflow velocity profile can be calculated by application of Womersley theory [20].
The influence of hematocrit (Hct) levels, plasma viscosity and the flow rate on the WSR and WSS can be assessed. For these purposes, we used a well-tested model, the Carreau-Yasuda model, for non-Newtonian viscosity and varied Hct within ranges, which were obtained from a group of 20 healthy young volunteers (Hct range: 0.346-0.506) [16, 25]. MRI acquisitions were performed in these young volunteers to obtain realistic flow rates during a cardiac cycle. In the FEM simulation, the flow and the plasma viscosity were varied within these realistic ranges.
A good similarity between MR-measurements and calculations was found for the curved tube phantom. Additional information for further analysis can probably be gathered from analysis of the secondary flows (vortices), which are also visible in the MR-data. The velocity profiles can be assessed and visualized individually. The MRI flow and velocity measurements were in good agreement with the calculated data. It can be concluded that flow(t) and velocity profiles can give a good impression of the similarity between measurements and calculations. This validation approach opens the possibility for future studies. In contrast to the curved tube model with smooth and fixed walls, *in vivo* geometries are not exactly known. For *in vivo* geometries, boundary conditions can probably be optimized using this method.
In summary, the methods presented and validated in this manuscript create new possibilities to apply patient-specific CFD calculations, such that individual and local Wall Shear Stress values can be assessed in clinical research.

**Acknowledgement**
Grant support: Netherlands Heart Foundation Grant 2000.119

**References**


1. Malek AM, Alper SL, Izumo S. Hemodynamic shear stress and its role in atherosclerosis. *JAMA* 1999;282:2035-2042

2. Gnasso A, Carallo C, Irace C. Association between intima-media thickness and wall shear stress in common carotid arteries in healthy male subjects. *Circulation* 1996;94:3257-3262

3. Irace C, Carallo C, Cresenzo A. NIDDM is associated with lower wall shear stress of the common carotid artery. *Diabetes* 1999;48(1):193-197

4. Jiang Y, Kohara K, Hiwada K. Low wall shear stress contributes to atherosclerosis of the carotid artery in hypertensive patients. *Hypert Res- Clin and Exp* 1999;22(3):203-207

5. Steinman DA., Rutt BK. On the nature and reduction of plaque-mimicking flow artifacts in black blood MRI of the carotid bifurcation. *MRM* 1998;39:635-641

6. Long Q, Xu XY, Collins MW, Griffith TM et al. The combination of magnetic resonance angiography and computational fluid dynamics: A critical review. *Crit Rev in Biom Engin* 1998;26(4):227-274

7. de Koning PJH, Schapp JA, Janssen JP et al. Automated segmentation and analysis of vascular structures in magnetic resonance angiographic images. *Magn Reson Med* 2003;50(6):1189-1198

8. Box FMA, van der Geest RJ, Spilt A et al. Automatic model-based contour detection and blood flow quantification in small vessels with velocity encoded magnetic resonance imaging. *Invest Radiol* 2003;38:567-577

9. Sethian JA (1996) A fast marching level set method for monotonically advancing fronts. Proc Nat Acad Sci USA 93:1591-1595

10. Westenberg JJM, van der Geest RJ, Wasser MNJM et al. Vessel diameter measurements in gadolinium contrast enhanced three dimensional MRA of peripheral arteries. *Magn Reson Imaging* 2000;18:13–22

11. de Vries M, de Koning PJ, de Haan MW et al. Accuracy of semiautomated analysis of 3D contrast-enhanced Magnetic Resonance Angiography for detection and quantification of aortoiliac stenoses. *Invest Radiol* 2005;40(8):495–503

12. Spilt A, Box FMA, van der Geest RJ, Reiber JHC et al. Reproducibility of total cerebral blood flow measurements using phase contrast Magnetic Resonance Imaging. *JMRI* 2002;16(1):1-5

13. Fleiss JL.The design and analysis of clinical experiments. John Wiley & Sons 1986:8-1

14. Box, FMA, van der Geest RJ, Rutten MCM et al. The influence of flow, vessel diameter and non-Newtonian blood viscosity on the Wall Shear Stress in a carotid bifurcation model for unsteady flow. *Invest Radiol* 2005;40(5):277-294

15. Segal G Ingenieursbureau SEPRA, Park Nabij 3, Leidschendam, the Netherlands

16. Gijsen FJH, Allanic E, Van de Vosse FN et al. The influence of non-Newtonian properties of blood on the flow in large arteries: unsteady flow in a 90 degrees curved tube. *J of Biomech* 1999;32(7):705-713

17. Matrai A, Whittington RB, Ernst E. A simple method of estimating whole blood viscosity at standardized heamatocrit. *Clin Hemorheol* 1987;7:261-265

18. Summers PE, Holdsworth DW, Nikolov HN et al. Multisite trial of MR flow measurement: Phantom and protocol design. *JMRI* 2005;21:620-631

19. Nichols WW, O'Rourke MF. McDonald's Blood Flow in Arteries. Theoretical, experimental and clinical principles. Fourth edition. Oxford University Press, Inc 1998:36-40

20. Womersley JR. An elastic tube theory of pulse transmission and oscillatory flow in mammalian arteries. Technical report, Wright Air Development Centre TR 1957:56-614

21. Rutten MCM. Fluid-solid interaction in large arteries. Eindhoven University of Technology, Eindhoven, the Netherlands 1998

22. Van de Vosse FN, Van Steenhoven AA, Segal A et al. A finite element analysis of the steady laminar entrance flow in a 90 curve tube. *Int J Num Meth In Fluids* 1998;9:275-287

23. Van der Geest RJ, Niezen RA, van der Wall EE et al. Automatic measurements of volume flow in the ascending aorta using MR velocity maps. *J Comput Assist Tomogr* 1998;22(6):904-911

24. Kellenberger CJ, Macgowan CK, Roman KS et al. Hemodynamic evaluation of the peripheral pulmonary circulation by cine phase-contrast magnetic resonance imaging. *JMRI* 2005;22:780-787

25. Cho YI, Kensey KR. Effects of the non-Newtonian viscosity of blood on flows in a diseased arterial vessel part. Part 1: steady flows. *Biorheology* 1991;28:241-262